Radar Backscatter from Breaking Waves in Gulf Stream Current Convergence Fronts

Scott R. Chubb, Arnold L. Cooper, Robert W. Jansen, Robert A. Fusina, Jong-Sen Lee, *Fellow, IEEE*, and Farid Askari

***Abstract*—Bright linear features have been observed in radar imagery taken near the Gulf Stream (GS) boundary on two separate occasions. In each case, these have been observed directly over strong current convergences. Progress has been made in understanding the origin of these signatures through simulations that incorporate environmental forcing from the winds and currents. These simulations significantly underestimate the backscatter unless wave-breaking (WB) effects are included at least approximately. Using a new, quasistatistical procedure that generalizes and quantifies earlier procedures for including WB effects, we have been able to successfully simulate the magnitude and behavior of these signatures. The approach combines the statistically based, composite model of radar backscatter with a deterministic feature model that relates backscatter from breaking waves to a particular geometrical model of a spilling breaker. This is accomplished using localized criteria, defined by local wave crest acceleration, to determine the probability of breaking, and by extending the feature model so that its unknown parameters may be evaluated directly from wave–current interaction calculations. The new approach provides an estimate of the critical crest acceleration of a potentially breaking wave, as a function of wind speed, that agrees with independent measurements.**

***Index Terms*— Gulf Stream, radar, wave-breaking, wave-current interaction.**

I. Introduction

PARTICULARLY bright radar signatures have been observed in imagery taken at the boundary of the Gulf Stream (GS) during both the first high resolution remote sensing (HIRES-1) experiment [1] and the GS 1990 (GS'90) experiment [2]. During GS'90, the signature was in the form of a bright line. In the HIRES-1 imagery, the signature was a bright meandering linear feature. In each case, ground truth information has revealed that the feature occurs directly over a strong current convergence.

In a previous study [3], [4], simulated radar imagery that incorporates the interaction of the small-scale surface waves with the underlying convergent current structure has been used to obtain a qualitative understanding of the origin of the two signatures. In both cases, an estimate of the magnitude of the signature was obtained from calculations that include wave-current interaction but neglect wave-breaking (WB) effects. However, in this study, the magnitude of each signature was underpredicted. This study provided bounds for WB-induced enhancements to each signature that are consistent with the experiment, using an approximate model of WB effects.

In the present paper, an improved electromagnetic backscatter approach that incorporates local WB effects is used to eliminate the unknown parameters that were used in the earlier work [3], [4]. The new approach, called the local wave-breaking criteria (LWBC) method, was inititally developed and tested, using a refined one-dimensional (1-D) model of the HIRES-1 surface currents [5]–[7] that included both the convergence and shear that were present in the vicinity of the signature. Some of the results from this earlier study are included in the present paper. These results show that it is possible to predict the magnitude ($\sim$11 dB) of the signature (relative to the ambient background), based on the LWBC method, in good agreement with measurement, where it was found [5], [6] that the signature varies in relative intensity over a range of values between 10 and 15 dB. Also, in the present paper, the LWBC approach is applied to the GS'90 signature, using a current model that is very similar to the one used in the earlier study [3], [4]. Again, quantitative agreement for the ($\sim$3 dB) enhancement observed in the radar return over the feature is obtained.

These calculations provide a quantitative explanation for the origin of the reduced magnitude in the GS'90 signature relative to its HIRES-1 counterpart and explain similarities between the two signatures. In particular, in both cases, the calculated maximal WB-induced effect is found to provide optimal agreement with experiment. In both cases, the magnitude of the signature is fixed by the maximum WB-induced enhancement, and this enhancement occurs when it is assumed that WB occurs when the local crest acceleration exceeds a critical value of $\sim$0.4 g ($g = 9.8$ m/s^2).

Specifically, the WB-induced enhancement is derived from the assumption that the probability of WB occurring can be equated with the probability that wave crest acceleration (or slope) locally exceeds some critical value Λ_c [7]–[10]. We illustrate that in the two very different signatures from HIRES-1 and GS'90; Λ_c-values are obtained that are very close in value. This occurs in the 1-D model of the HIRES-1 rip signature [5]–[7] and in a more sophisticated two-dimensional (2-D) model [8], [9] discussed in the next paragraph. These Λ_c-values are in good agreement with comparable values obtained both in wave tanks and field experiments [7]. Thus, these results not only illustrate that, by including WB effects, good quantitative agreement with experimental findings for the magnitudes of the radar signatures can be obtained, but also that these WB effects provide evidence in support of

Manuscript received May 19, 1998; revised September 9, 1998. This work was supported by the Naval Research Laboratory High Resolution Remote Sensing Advanced Research Initiative, through the Office of Naval Research.

The authors are with the Remote Sensing Division, Naval Research Laboratory, Washington, DC 20375-5351 USA (e-mail: chubb@ccf.nrl.navy.mil).

Publisher Item Identifier S 0196-2892(99)04335-1.

the hypothesis that critical crest acceleration criteria can be used to predict the onset of WB. This is the first time, to our knowledge, that values for Λ_c have been inferred using remote-sensing microwave imaging techniques.

The studies of the meandering HIRES-1 rip signature and line-shaped GS'90 signature described above both involve 1-D models of the surface currents, which were represented either as a simple current convergence [3], [4] (applicable to both HIRES-1 and GS'90 signatures) or (in the case of HIRES-1 in [5] and [6], and for GS'90 in the present work) as a current convergence in the presence of a shear [3]–[7], [10]. These 1-D models of the currents cannot be used to understand a number of effects associated with the HIRES-1 rip signature because the resulting estimates are applicable to regions where the effects of changes in the direction of the rip are not pronounced. In fact, the strength of the rip signature varied considerably ($\sim$10–15 dB) as a function of position and was greatest in the "cusp-like" regions associated with positions where changes in the meander were sharpest. In an earlier study [11], it was found qualitatively that this pattern of variation in signal strength, in which the largest return was found to occur in the regions where the direction of the signature changes most sharply, could be obtained using the composite backscatter (CB) model. This was accomplished using wave spectra derived from wave-current interaction calculations involving currents constructed from a sinusoidally varying 2-D functional form. The resulting range of values of the radar cross section (RCS) within the rip, however, calculated from the model, was significantly larger than what was observed in the experiment, and the associated backscatter exhibited a nonphysical dependence on look-angle that was not present in the experiment.

As a final illustration of the importance of WB effects, in this paper, we apply the LWBC to this 2-D current model. We find that, by including WB, very good agreement with the experiment is obtained for the magnitude of the signature across and within the rip. In particular, it is found that, by including WB, the deficiencies that are found when the CB model is used alone are eliminated. Thus, within the rip, when WB effects are included, the location of maximal and minimal cross section, and the manner in which RCS varies within the meander, all agree well with the experiment. Also, incorporation of these effects into the RCS modeling eliminates the nonphysical dependence on look-angle that occurs when the CB model is used alone.

This paper summarizes the results of applying the LWBC method in the analysis of the GS'90 and HIRES-1 radar signatures. It also includes a discussion of the relationship between the LWBC method and an earlier (less quantitative) procedure, called the sparse breaker model (SBM) [3]–[6], for including WB effects. The organization of the paper is as follows. In Section II, the procedure for performing the RCS simulations is reviewed. This includes a review of the procedures for performing the calculations of wave spectra, based on wave-current interaction calculations, and for modeling the currents associated with both radar signatures. This is followed by a review of the manner in which RCS is calculated, based on the wave spectra that result from the wave-current interaction calculations, and detailed discussions of the LWBC procedure for including WB corrections and the manner in which the adjustable parameters of the earlier SBM can be obtained from the LWBC. In Section III, the results of the simulations are presented. The final section summarizes important conclusions of the study.

II. Method

A. Hydrodynamic Calculations

Previous simulations [3]–[7], [10], [11] of RCS of the HIRES-1 rip feature and GS'90 bright line feature [3], [4], [12] have been based on wave-current interaction calculations of wave height spectra $F(\boldsymbol{r}, \boldsymbol{k}, t)$, as a function of the time t, and the 2-D wave-vector $\boldsymbol{k}$ at locations $\boldsymbol{r}$ on the ocean surface. In these calculations, $F(\boldsymbol{r}, \boldsymbol{k}, t)$ is derived from the intrinsic angular wave frequency $\omega_o(k)$ [$\equiv(gk+T/\rho k^3)^{1/2}$, $k \equiv |\boldsymbol{k}|$, $\rho =$ density of sea water, and $T \equiv$ surface tension] and wave action spectral density $N(\boldsymbol{r}, \boldsymbol{k}, t) \equiv \omega_o(k)/kF(\boldsymbol{r}, \boldsymbol{k}, t)$. In the initial 1-D model calculations [3], [4], [12], $N(\boldsymbol{r}, \boldsymbol{k}, t)$ and $F(\boldsymbol{r}, \boldsymbol{k}, t)$ were derived using one (y-dependent) northward current component [3], [4], [12] V of the form

$$V(y) = -\frac{\delta V}{2} \tanh\left(\frac{y}{\delta y}\right). \tag{1}$$

In the model of the GS'90 feature [3], [4], [12], the signature occurs when $y = 0$ and $|\partial V/\partial y| \approx 0.002$ s^{-1}. Appropriate values are $\delta V = 0.2$ m/s and $\delta y = 50$ m, and $V(y)$ was evaluated over the range -400 m $< y <$ 1000 m. It was also shown [3], [4], [12] that, for the 8-m/s wind speed that was present [12], the magnitude of the signature was relatively insensitive to variations in δV over the range of values 0.2 m/s $< \delta V <$ 0.4 m/s. In the present paper, we model the GS'90 feature using (1) with a slightly different value for $\delta V = 0.25$ m/s and the previous value for δy to obtain V. In the model, we also introduce a slight shear through an eastward current $U \equiv U(y)$, which is consistent with measurements performed during the experiment [9]. We do this using

$$U(y) = \tanh\left(\frac{y}{\delta y}\right) \times 0.05 \text{ m/s}. \tag{2}$$

Additional modeling of RCS (beyond the calculations presented in [3] and [4]) of the HIRES-1 rip feature [7], [10], also included both U and V components of the current, but again, using the important simplifying assumption that the only spatial dependence in the currents occurs in one direction: $V \equiv V(y)$, and $U \equiv U(y)$ [7], [10]. As opposed to the model used in [3] and [4] in the later calculations, a considerably more sophisticated current structure was used, derived from the time evolution of subsurface currents that are initiated from a dynamically unstable configuration, involving denser GS water, coming into contact with less dense shelf water. One-dimensional modeling of WB effects for the HIRES-1 rip feature presented in this paper are derived from these calculations of F, based on this later current model.

Because the currents in these previous studies only include a dependence on y, it is not possible from these calculations to infer information about the behavior of the RCS in regions where strong spatial variation in the rip occurs in both the $\boldsymbol{x}$-

and $\boldsymbol{y}$-directions. To investigate this point, we have employed a different model that was used previously [11] in RCS calculations based on the CB model. In the results presented below, we have extended these earlier calculations by incorporating WB effects in the RCS calculations, using the LWBC model. The associated 2-D model for the currents is defined by $U = 0$, and $V = V(\boldsymbol{x}, \boldsymbol{y})$, with

$$V(x, y) = -\frac{\delta V_{2d}}{2} \tanh\left[\frac{\boldsymbol{y} - \boldsymbol{x_o} \sin\left(\frac{2\pi x}{\lambda}\right)}{\delta y}\right]. \quad (3)$$

Here, the values for $\delta V_{2d} = 0.6$ m/s and $\delta y = 30$ m are used to mimic the convergence observed [5], [6] during HIRES-1. (These values were also used previously [3], [7], [10], [11].) The remaining parameters $\boldsymbol{x_o} = 300$ m and $\lambda = 1500$ m were inferred from radar imagery [8]–[10]. Using these current models, N is derived from the steady-state form [8], [9] of the wave action equation

$$\nabla_{\boldsymbol{k}}\omega \cdot \nabla_{\boldsymbol{x}} N - k_{\boldsymbol{x}}\left[\frac{\partial U}{\partial x}\frac{\partial N}{\partial k_{\boldsymbol{x}}} + \frac{\partial U}{\partial y}\frac{\partial N}{\partial k_{\boldsymbol{y}}}\right] - k_y\left[\frac{\partial V}{\partial y}\frac{\partial N}{\partial k_y} + \frac{\partial V}{\partial x}\frac{\partial N}{\partial k_x}\right] = -\beta\frac{N}{N_o}(N - N_o). \quad (4)$$

Here $\omega = \omega_o + k_x U + k_y V$, and β and N_o, respectively, are the Plant wind growth rate and Bjerkaas–Riedel equilbrium wave action that were used previously [1]–[4].

As before [7], [10], RCS values are determined from F, using the CB model, without the small slope approximation [7] that was used in [3] and [4]. WB effects are investigated using the LWBC approach [7], [10] and (in the case of the HIRES-1 feature) the SBM developed in [3] and [4]. In [7], the underlying assumptions of the LWBC method and the procedure for applying it are presented. The discussion presented there, however, is incomplete. In what follows, a more complete description is presented that includes a procedure for using the LWBC method to derive the unknown adjustable parameters associated with the SBM.

B. Radar Backscatter: The LWBC Method

In the LWBC, the RCS is derived probabilistically, by combining the CB model RCS (suitably weighted so that it applies in locations where breaking does not occur) with an approximate feature model of a breaking wave, using the probabilities $P(\boldsymbol{r})$ or $(1 - P(\boldsymbol{r}))$ for WB to occur or not to occur at $\boldsymbol{r}$. Specifically, the RCS is derived from

$$\sigma_{tot}^{sp} = (1 - P(\boldsymbol{r}))\sigma_{cb}^{sp} + P(\boldsymbol{r})\sigma_{wb}^{sp} \quad (5)$$

where σ_{wb}^{sp} denotes the specific, average cross section that is attributed to breaking processes. Also, σ_{cb}^{sp} (which is assumed to approximate the RCS per unit area in the absence of WB) is evaluated from the standard, specific RCS expressions of the CB model [13], [14]. (In order to obtain an accurate representation for X-band and higher microwave frequencies, this is done without the small slope approximation that is frequently used [7].) In the LWBC method, $P(\boldsymbol{r})$ and σ_{wb}^{sp}, respectively, are inferred from crest acceleration Λ and wave-height variance values that are derived from F.

To accomplish this, a specific model for constructing σ_{wb}^{sp} is introduced in which the predominant source of backscatter from breaking waves is assumed to be from a dominant geometrical (plume-like) shape. Then, a procedure is constructed for inferring parameters that define the vertical and horizontal extent of this average shape, based on the statistical information provided by the wave height spectrum.

Once a particular parameter set has been inferred, σ_{wb}^{sp} is determined using a feature modeling approach due to Wetzel [15], [16]. The necessary geometrical information associated with σ_{wb}^{sp} is obtained using the wave action. This is a new approach that effectively marries the more restrictive, deterministic method applied by Wetzel with a statistical scheme. In particular, as outlined below, wave slope spectra are constructed from the wave action calculations. These are used to determine average information about potential breaking processes and in conjunction with local WB criteria to infer $P(\boldsymbol{r})$. In the process of deriving $P(\boldsymbol{r})$ in this way, estimates are obtained of effective average values of all of the additional geometrical parameters required by Wetzel's model. (This eliminates the unknown geometrical parameters of Wetzel's theory, which previously either have been treated as adjustable parameters or used to develop a qualitative understanding of WB-induced enhancements.) An additional result of this alternative approach is that it introduces frequency, polarization, and environmental information associated with the local WB environment that is not present in the original SBM.

Wetzel [15], [16] has modeled radar return from WB processes by assuming that a particular geometry can be used to derive the resulting backscatter. The choice of geometry is based on a particular geometrical form (or "feature") that resembles the shape of a spilling breaker obtained in the Plume model [17]. The associated feature is derived from a second (raindrop) feature model due to Wetzel. In Wetzel's raindrop feature model, the sea surface manifestation of rain is approximated by a feature consisting of a donut-like structure that is elevated by an amount H (referred to by Wetzel as the "slosh region") and a receding dimple (of depth $-H$). The donut has diameter L. In Wetzel's spilling breaker model, the breaker is modeled using a portion of the donut and dimple, defined by passing a chord of length L through the inner circle of the "slosh region." Fig. 1 shows plots of the features associated with both (raindrop and spilling breaker) models. To simplify the analysis, we approximate the feature associated with the spilling breaker using the raindrop model feature. This approximation eliminates anisotropies associated with edge effects, while retaining the (specular) scattering effects that are believed to be important [15], [16]. This approximation leads to an important simplification, involving the elimination of the unknown length scale L, which is discussed below.

When the short-wavelength (physical optics) approximation ($2\pi H/\lambda \gg 1$, where $\lambda \equiv$ radar wavelength) applies, Wetzel's expression for the total cross section from an individual WB σ_{WB} (based on Wetzel's raindrop model) can be expressed using the two length scales H and L

$$\sigma_{\mathrm{WB}} = \tfrac{1}{2} k_o H L^2 F_x^2. \quad (6)$$

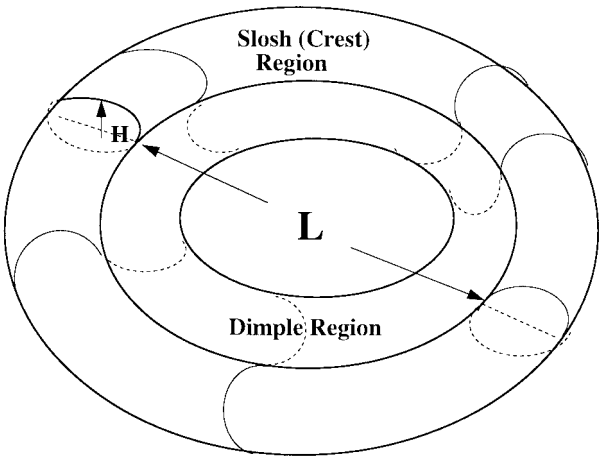

(a)

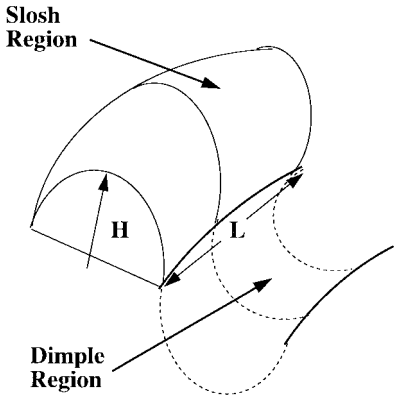

(b)

Fig. 1. Plots of the "Feature Model" geometries for the (a) "Raindrop" and (b) "Spilling Breaker" models defined by [15] and [16]. Solid lines are used to show regions that extend above and immediately to the water surface. Dashed lines show regions below the water surface.

Here, $k_o = 2\pi/\lambda$, and F_X is the "surface proximity function," defined by

$$F_X = \left| e^{ik_o H \cos(2\theta_g)} + R_X e^{ik_o H} \right| \tag{7}$$

where X denotes the polarization of the incident radiation, θ_g is the local grazing angle, and $R_X \equiv R_X(f, \theta_g)$ is the complex reflection coefficient of an incident wave of frequency f and grazing angle θ_g. Consistent with Wetzel's model [15], [16], it is assumed in (6) that $k_o H$ is much larger than unity.

In [15], a tabulation is provided of the proximity function F_X, based on the values of R_X, given by Saxton and Lane [18]. Although for values of $\theta_g < 30°$, considerable variation of F_X occurs at X-band, for the larger values of θ_g of interest in the present work, F_X^2 approaches unity, so that

$$\sigma_{wb} \approx \tfrac{1}{2} k_o H L^2. \tag{8}$$

The area q of a breaking wave that applies to the circular plume-like structure of (6) and (8) is given by

$$q \equiv \frac{\pi L^2}{4} \approx L^2. \tag{9}$$

When the illuminated area of the radar is Q, locally, the breaking probability $P(\boldsymbol{r})$ may be equated with the average, local fractional coverage of breaking waves q/Q (an equality that applies when the spatially and time-averaged probabilities are equivalent). It follows that, when an average specific cross section defined by $\sigma_{wb}/Q \equiv P(\boldsymbol{r})\sigma_{wb}^{sp}$ is used, we may define $\sigma_{wb}^{sp} \equiv \sigma_{wb}/q$ using a local mean value for $H \equiv H(\boldsymbol{r})$ that is determined from an estimate of the local height $H(\boldsymbol{r})$ of a breaking wave. This is made possible by an important cancellation that results from the fact that, as a consequence of (8) and (9), σ_{wb} is proportional to q. Combining (8), (9), and the definition of σ_{wb}^{sp}, we find

$$\sigma_{wb}^{sp} \approx \frac{k_o H(\boldsymbol{r})}{2} \tag{10}$$

where the value of $H(\boldsymbol{r})$ is estimated from the local wave field, as explained below. In this way, the dependence on the unknown length scale L can be eliminated. In the next section, we illustrate an alternative procedure for estimating $P(\boldsymbol{r})$ that is independent of q and Q, so that we can evaluate (10) and at the same time provide information about the unknown quantity q. Substituting (10) into (5), we find

$$\sigma_{tot}^{sp} = (\sigma_{cb}^{sp}) \times (1 - P(\boldsymbol{r})) + \frac{P(\boldsymbol{r}) k_o H(\boldsymbol{r})}{2}. \tag{11}$$

C. Local Breaking Probabilities $P(\boldsymbol{r})$ and Heights $H(\boldsymbol{r})$

To determine $P(\boldsymbol{r})$, it is necessary to establish a critical value $\Lambda = \Lambda_c$ of the crest acceleration, beyond which breaking is assumed to occur with 100% certainty. This assumption is based on a suggestion given by Snyder and Kennedy (SK) [8], [9] in which $P(\boldsymbol{r})$ is equated with the probability $P_{\Lambda c}$ that, at the point $\boldsymbol{r}$, the local crest acceleration $a(\boldsymbol{r})$ exceeds a critical value Λ_c. SK assume that the ocean is homogeneous and that the wave-height obeys Gaussian statistics (meaning that $a(\boldsymbol{r})$ is uniformly and normally distributed), so that $P_{\Lambda c}$ may be computed globally from the variance of a that results from the short-time ($\delta t \to 0$) and small-distance ($\delta r \to 0$) limit of the acceleration auto-correlation function $M_4(\delta r, \delta t)$, defined by

$$M_4(\delta \boldsymbol{r}, \delta t) = \langle a(\boldsymbol{r}, t) a(\boldsymbol{r} + \delta \boldsymbol{r}, t + \delta t) \rangle = \int_0^\infty k\, dk \int_{-\pi}^{\pi} d\theta e^{(i(k \cdot \delta \boldsymbol{r} + \omega \delta t)} F(\vec{k}, \omega(k)) \omega^4(k). \tag{12}$$

We have generalized this approach slightly, based on two observations: 1) although in the results developed by SK, the WB process is assumed to be stationary and homogeneous globally, it is only necessary to assume that the process be stationary and homogeneous locally, and 2) it is assumed that the short-time and small-distance limit of M_4 can be derived using an acceleration–acceleration correlation function that results from the spectral density associated with the solution of the wave action equation. The criteria for breaking in the presence of currents are identified using acceleration information provided by the solution of the wave action equation, based on criteria due to SK. (Also, these criteria are extended using the assumption that they apply in a spatially homogeneous fashion locally, but not globally.)

In the present case, breaking phenomena appear to have been localized in the vicinity of the GS'90 feature [12] and

HIRES-1 rip [1]. The extension of the globally homogeneous results of SK to the locally homogeneous case considered here involves writing a (spatially dependent) expression for the probability $P(\boldsymbol{r})$ for breaking to occur at each point $\boldsymbol{r}$

$$P(\boldsymbol{r}) = \frac{1}{\sqrt{(2\pi D_4^{\boldsymbol{r}})}} \int_{\Lambda_c}^{\infty} da \, \exp\left(\frac{-a^2}{[2D_4^{\boldsymbol{r}}]}\right). \tag{13}$$

Here, because the process is assumed to be homogeneous locally, an explicit dependence on position is included (through the "$\boldsymbol{r}$" superscript) in the local acceleration variance $D_4^{\boldsymbol{r}}$, which is constructed by evaluating $M_4(0, 0)$ at the point $\boldsymbol{r}$

$$D_4^{\boldsymbol{r}} = M_4(0, 0)|_{(\boldsymbol{r})}. \tag{14}$$

Nonphysical numerical instabilities may result when (12) is evaluated because a number of the commonly used equilibrium height spectra F_o do not fall off sufficiently rapidly with increasing wavenumber to ensure that the integral in (12) is bounded for large values of k. Specifically, for large k, the prefactor of F that appears in (12) asymptotically approaches k^7, which is poorly defined unless F asymptotically decreases faster than k^{-8}. This clearly is not the case when (4) is derived using choices for N_o that are defined by many of the more commonly used equilibrium wave spectra (e.g., in the Phillip's spectrum, $F \sim k^{-4}$ as $k \to \infty$). The Bjerkaas–Riedel equilbrium spectrum [19] used here, however, does fall off sufficiently rapidly to ensure that the integral is well defined. Despite this fact, there are a number of reasons to adopt a strategy in which the large wave-vector limit of (12) is cut off at some finite value: 1) measurements of spectra and the underlying assumptions regarding application of spectra to obtain acceleration variance are suspect in the short wavelength limit and 2) the electromagnetic model for backscatter associated with (11) is not consistent with including wave vectors that are larger than ~1/3 the Bragg wave vector k_{Bragg} [defined by $k_{\text{Bragg}} = 2 * k_o \sin(\theta_{\text{inc}})$, $\theta_{\text{inc}} \equiv$ angle of incidence].

SK [8], [9] investigated the first of these justifications for applying (12) with a finite wave vector cut off through numerical tests and comparisons with WB probability measurements. In the radar backscatter problem, a more rigorous justification, based on the second reason, is applicable. In particular, in the CB approach, scattering is treated through a two-scale model in which the shorter waves are normally distributed and evolve independently from the wind and the underlying currents; while the longer waves evolve according to the wave action (4). Partial formal justification of the two-scale model procedure is provided by Thompson [20]–[22], who has shown that (in the case of a perfectly conducting ocean surface) the picture can be rigorously derived through an expansion of the longer wave height–height autocorrelation function in which higher order moments beyond those that enter as the square of the wave vector are neglected. A consistent picture that preserves these requirements of the two-scale model by maintaining only terms of this order in the evolution of time-dependent quantities is obtained when the k-integration of (12) is restricted so that all values beyond the upper limit value $k_u \equiv 2\pi/\lambda_u$ (with $\lambda_u \gtrsim 0.05$ m) are excluded. Then, as observed by Lyzenga [23] and Lyzenga and Bennett [14], because the longwave gravity wave dispersion relationship $\omega_o^2(k) = gk$ is valid for the resulting range of k-values that are included in the k-integration in (12), it follows that $D_4^{\boldsymbol{r}}$ can be computed from the slope spectrum variance $\langle S_x^2 + S_y^2\rangle|_{\boldsymbol{r}}$:

$$D_4^{\boldsymbol{r}} \approx g^2 \langle S_x^2 + S_y^2\rangle|_{\boldsymbol{r}} \tag{15}$$

where

$$\langle S_i^2\rangle|_{\boldsymbol{r}} \equiv \int_0^{k_u} k \, dk \int_{-\pi}^{\pi} d\theta k_i^2 F(k, w(k), \boldsymbol{r}). \tag{16}$$

Here, $k_i = k\cos(\theta)$ or $k_i = k\sin(\theta)$ when, respectively, $i = x$ or $i = y$. Since $D_4^{\boldsymbol{r}} \propto \langle S_x^2 + S_y^2\rangle|_{\boldsymbol{r}}$, at each point $\boldsymbol{r}$, $D_4^{\boldsymbol{r}}$ becomes large or varies significantly when the average slope variance $\equiv \langle S_x^2 + S_y^2\rangle|_{\boldsymbol{r}}$ becomes large or varies significantly. This is a reasonable approximation, especially when WB occurs predominantly from waves that are of moderate ($\gtrsim$0.05 m) wavelength. Because $D_4^{\boldsymbol{r}} \propto \langle S_x^2 + S_y^2\rangle|_{\boldsymbol{r}}$, it follows that the assignment of a critical crest acceleration based on this procedure is equivalent to the assignment of a critical waveslope and breaking probability is equal to the probability of exceeding a critical slope.

Based on Longuet–Higgins's argument [24], for the limiting case involving Stokes waves, that breaking occurs when crest accelerations exceed 0.5 g, an approximate upper bound $\Lambda_c^{\max}$ for breaking can be inferred through the requirement

$$\sqrt{D_4^{\boldsymbol{r}}} > \Lambda_c^{\max} \approx 0.5 \text{ g}. \tag{17}$$

In practice, we have estimated values of Λ_c, by maximizing the WB-induced enhancement to σ_{tot}^{sp}. Empirically, as discussed in Section III, not only do we find that $\Lambda_c < \Lambda_c^{\max}$, but that $\Lambda_c \simeq 0.4$ g for all of the cases that we have considered. We also find that these values of Λ_c are consistent with values obtained in wave-tank studies and in the field. As a consequence, the application of the procedure in the present study involving currents provides a link for relating crest acceleration WB criteria to more general situations.

Estimates of $H(\boldsymbol{r})$ are derived from calculations of an average rms deviation (variance) of the mean relative elevations of breaking and nonbreaking waves. This requires an assumption about the regions of the spectrum that are involved with breaking waves. We accomplish this by calculating the associated deviations in height from different portions of the spectrum F. Because H is an average physical deviation that results from realizations of the surface, we estimate it using a portion of the average total deviation in height $H_{tot} \equiv (2\langle\eta^2\rangle)^{1/2}$, where $\langle\eta^2\rangle$ is the variance defined by F. [Here, as discussed by Kinsman [25], the factor of two that applies in this definition occurs because the wave-height spectrum F is restricted to cases involving positive frequencies $\omega(k)$.] An upper bound for H is provided by including all spectral components in the evaluation. As in the SBM, however, we construct H using the smaller subset of components defined by the portion of the spectrum where significant WB occurs. This portion of the spectrum is defined by the region $k_2 < k < k_1$ and $\theta_1 < \theta < \theta_2$, where N is significantly different than N_o. Then, we obtain the following:

$$H(\boldsymbol{r}) \equiv \left[2 \times \sum_{k=k_1}^{k=k_2} \sum_{\theta=\theta_1}^{\theta=\theta_2} F(k, \theta, x, y) k \Delta k \Delta\theta\right]^{1/2}. \tag{18}$$

In the evaluation of (12) and (15), we have used an upper k-integration cut off k_u defined by $2\pi/k_u = \lambda_u = 7.95$ cm. This choice falls within the range ($\lambda_u > 0.05$ m), where (27) applies. The choice is also consistent with the radar parameters (9 Ghz, $\theta_{\rm inc} = 37.5°$) that apply to the HIRES-1 rip with the value of the upper limit dynamical value k_d (Lyzenga and Bennett [14]), through an equality $k_u = k_d = k_{\rm Bragg}/3$ that has been imposed for convenience. We have estimated $H(x, y)$ using (18) and the following values for k_1, k_2, θ_1, and θ_2: $k_1 \equiv 1/(4\pi)$ m^{-1} $< k < 3/\pi$ m^{-1} $\equiv k_2$, $\theta_1 \equiv -45° < \theta < 45° \equiv \theta_2$ centered about the maximum variation in $N - N_o$. We selected these values to be consistent with the assumptions of the earlier application of the SBM (as discussed in [3] and [4]).

D. Relationship Between LWBC and SBM Procedures

In the earlier 1-D calculations of radar signatures from fronts, the SBM was used [3], [4] to study WB-induced enhancements from calculations of the ratio of the total specific RCS σ_{tot}^{sp} to its mean, ambient value $\sigma_{tot}^{sp}(0)$. Because the calculations were 1-D and involved WB effects that were localized primarily in the vicinity of fronts, it was possible to do this using a scheme involving a single adjustable parameter α^o, defined by the ratio of the magnitudes of contributions to the RCS from WB and non-WB scattering processes in regions far from the front, where the ambient (background) RCS is found. Thus, in the SBM

$$\frac{\sigma_{tot}^{sp}}{\sigma_{tot}^{sp}(0)} \equiv \frac{\sigma_{tot}}{\sigma_{tot}(0)} \equiv \frac{\chi_{\rm CS} + \alpha_o \chi_{\rm WB}}{1 + \alpha_o}. \tag{19}$$

Here, $\chi_{wb}(\boldsymbol{r})$ and $\chi_{cb}(\boldsymbol{r})$ are the WB and composite scatter enhancements, defined, respectively, by the ratios of contributions from WB and non-WB scattering to the cross section at the location $\boldsymbol{r}$ to the comparable contributions to the cross section at the position where the cross section obtains its ambient value. The additional quantity α^o is the adjustable parameter.

Using (5), α^o can be rewritten in the form

$$\alpha^o \equiv \frac{\sigma_{wb}^{sp}(0) P(0, 0)}{\sigma_{cb}^{sp}(0)(1 - P(0, 0))} \tag{20}$$

where $\sigma_{wb}^{sp}(0)$ is given by the right side of (11) with $H(\boldsymbol{r})$ defined by its value at the extreme southern edge of the hydrodynamic calculation (which corresponds to the location of the ambient condition), $\sigma_{cb}^{sp}(0)$ refers to the specific composite scattering cross section and $P(0)$ is the probability of breaking, both evaluated at the same (extreme southern) ambient-condition-boundary location.

Because the parameter α^o depends on both cross-section information and $P(0)$, by construction, when $\sigma_{wb}^{sp}(0)/\sigma_{cb}^{sp}(0)$ is held fixed, each value of Λ_c, which uniquely defines the value of $P(0)$, also defines the value of α^o. In particular, in the LWBC, $\sigma_{wb}^{sp}(0)/\sigma_{cb}^{sp}(0)$ is defined by (10) and the CB model RCS expressions, so that this ratio is always independent of Λ_c. Thus, in the LWBC procedure, the only way that α^o is allowed to change is through $P(0)$; this is allowable when Λ_c has not been specified through a procedure in which this parameter is allowed to vary. Such a procedure for varying α^o is different than the one that occurs in the SBM, where α^o is, however, allowed to vary in order to identify bounds associated with WB [3], [4]. This kind of variation, by assumption, requires that the dissipated power in the ambient region be held fixed, meaning $P(0)$ is also held fixed. (By construction, the SBM assumes that relative to the ambient region values, at points $\boldsymbol{r}$ within the front, the values of $P(\boldsymbol{r})$, power from wave dissipation [3], [4] [defined by the wave action source function], and WB contributions to RCS are all proportional to each other. This assumption applies in an average sense when the density of breaking waves is sufficiently sparse.) As a consequence, when α^o is varied in the SBM, to be consistent with the assumptions of the model, $\sigma_{wb}^{sp}(0)/\sigma_{cb}^{sp}(0)$ is being varied. This is not allowed in the LWBC since the contributions to the RCS from WB and CB are fixed as a result of the electromagnetic scattering model that is used. This result illustrates one reason the LWBC has greater predictive power than the SBM: the SBM omits geometrical effects that are included [through the dependence of σ_{wb}^{sp} on $H(\boldsymbol{r})$ in (10)] in the LWBC.

Also, the LWBC and SBM definitions of $P(\boldsymbol{r})$ are different. But since the SBM defines $P(\boldsymbol{r})$ only relative to an undetermined constant $(P(0))$, it is possible as an ansatz to use the $P(\boldsymbol{r})$, as defined by the LWBC procedure, to determine $\chi_{wb}(\boldsymbol{r})$ and $\chi_{cs}(\boldsymbol{r})$. As a result

$$\chi_{wb}^{\rm SBM}(\boldsymbol{r}) = \frac{P(\boldsymbol{r})}{P(0)} \tag{21}$$

and because the SBM omits the dependence of σ_{wb}^{sp} on $H(\boldsymbol{r})$ that appears in (10), in the LWBC, it is appropriate to introduce a comparable quantity $\chi_{wb}^{\rm LWBC}(\boldsymbol{r})$, that is defined by the ratio of the WB contribution at the point $\boldsymbol{r}$ to the background (ambient) WB contribution

$$\chi_{wb}^{\rm LWBC}(x, y) \equiv \frac{P(\boldsymbol{r})\sigma_{wb}^{sp}(x, y)}{P(0)\sigma_{wb}^{sp}(0)} = \frac{P(\boldsymbol{r})H(\boldsymbol{r})}{P(0)H(0)}. \tag{22}$$

Here, $H(0)$ is the value of the height $H(\boldsymbol{r})$ evaluated at the extreme southern (ambient-condition-boundary) location. By combining the last two equations, we find

$$\chi_{\rm WB}^{\rm LWBC}(x, y) \equiv \frac{\chi_{\rm WB}^{\rm SBM}(x, y) H(\boldsymbol{r})}{H(0)}. \tag{23}$$

Viewed in terms of operative definitions, this last equality provides a test of the approximate equality between $P(\boldsymbol{r})$ that is determined from the LWBC and the SBM breaking probability which results from the requirement that it be proportional to the wave dissipation power.

III. Results

A. The HIRES-1 Rip Feature, and Motivation for Including WB Effects

Fig. 2 shows X-band imagery of the HIRES-1 rip feature. It appears as a pronounced (~10–15 dB) increase in cross section, along the meandering line-shaped feature (colored primarily in red) that extends several kilometers, predominantly in the east–west direction. Two important points are that 1) independent evidence [1], [12] exists that WB was present in the vicinity of both this signature and the GS'90 feature, suggesting that WB effects possibly are involved in the associated

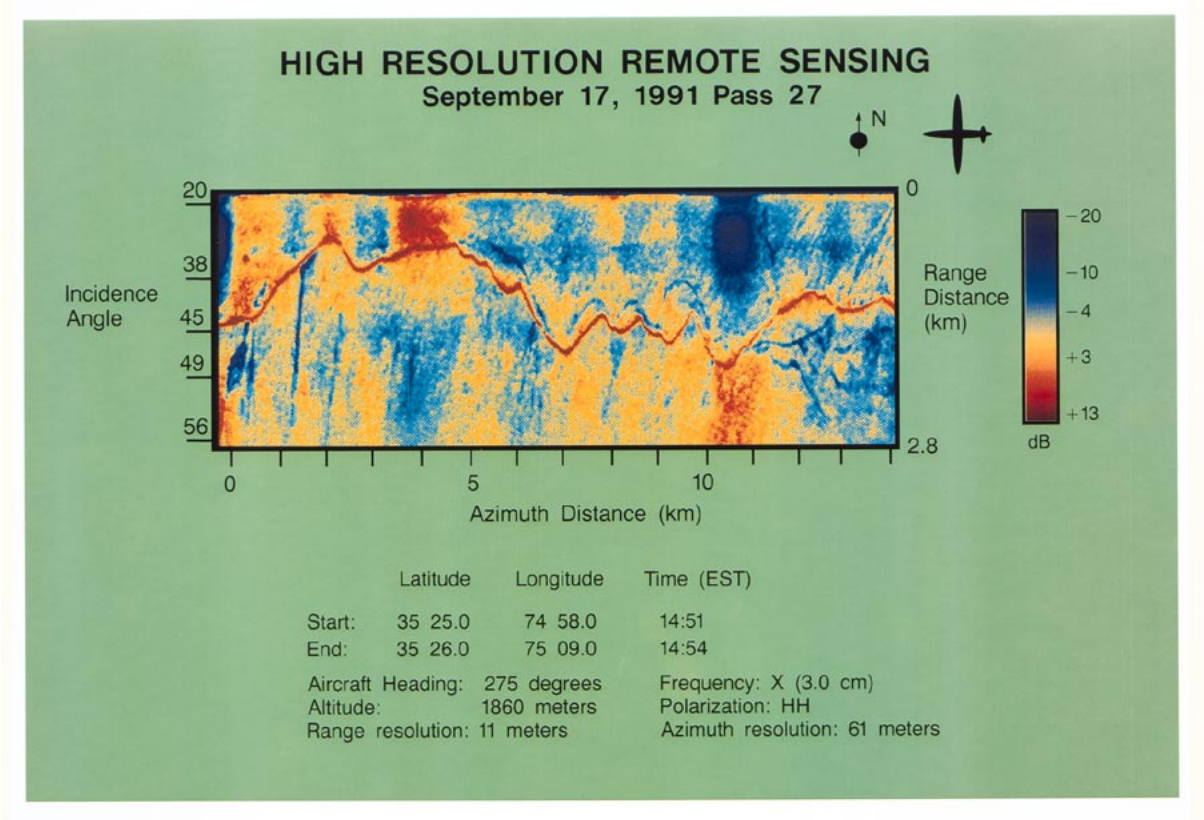

Fig. 2. Real aperture radar (RAR) image of HIRES-1 feature from airborne measurements by Askari [5], [6] performed off the coast of Cape Hatteras, NC, during the first NRL HIRES-1. The RCS is plotted using a pseudocolor scale that varies continuously between extreme blue shading, corresponding to extremely low (−20 dB) values of the RCS (relative to its ambient, average value), to extreme red shading, corresponding to the extremely high (13 dB) values (relative to the ambient). (The ambient value of the RCS occurs when the shading is yellow.) Relative to the ambient RCS value (shown in yellow), along paths that traverse the rip, the RCS variation is between ∼10 and 15 dB immediately over the rip, relative to its value immediately to the north and south of the rip. The direction and orientation of the flight path is represented through the schematic plot of an airplane, immediately above and to the right of the extreme upper right corner of the image.

electromagnetic backscatter, and 2) simulations based only on the CB model, which do not include WB, do not quantitatively predict the signature that is imaged in Fig. 2. In two 1-D models [3], [4], [7]–[9], the signature is simply underpredicted (by ∼6 dB); when the more sophisticated 2-D model is included [11], the maximum magnitude of the signature is obtained, but the range of variation is overestimated by ∼5 dB and a nonphysical dependence on look-angle is obtained. In this section, we illustrate that it is possible to correct these deficiencies in both the 1-D and the 2-D models by including WB effects.

Besides providing the correct range of variation of the signature, the 2-D modeling illustrates an additional trend: the relative maxima and minima in radar backscatter from the signature and the manner in which RCS varies within the signature, as a function of its location, qualitatively agree. In particular, as can be seen from Fig. 2, the largest RCS values are obtained at the locations of large curvature where the signature meanders significantly (i.e., where the direction of the signature changes significantly). As we will see, it is possible to obtain this behavior in simulations that are based on the hydrodynamic calculations associated with applying (3) and (4).

B. 1-Dimensional Model Results:

We begin by examining the improvements that result when WB is included in the 1-D model [7], [10] of the HIRES-1 rip feature. The surface currents for this model are derived from the time evolution of the subsurface current structure. The resulting surface currents, current gradients, and RCS are plotted for a representative time from this simulation in Fig. 3. In the top panel, the currents that flow across (solid line) and parallel to (dashed line) the front are shown. Here, the across-front current V is directed to the north (in the y-direction); the along-front current $(= -U)$ is directed in the westward direction. The comparable strain rate $\partial V/\partial y$ (solid line) and shear (dashed line), defined by $\partial U/\partial y$, are also shown. (The procedure for simulating the surface currents, shear and strain, which is based on a detailed 2-D calculation of the subsurface flow, is given in [7].) The bottom panel includes plots of the corresponding RCS across the feature, based on the CB model (dashed line) alone, and after incorporating the WB correction (solid line) that results from application of the LWBC method. The largest enhancement occurs at the location of the largest convergence (most negative cross-front divergence). In the model, this is the location of the signature. [Here, and in all of the 1-D calculations, the enhancement is expressed in decibels: RCS $\equiv 10 * \log_{10}(\sigma_{tot}^{sp}/\sigma_{tot}^{sp}(0))$, where $\sigma_{tot}^{sp}(0)$ is the ambient boundary value of σ_{tot}^{sp} defined by the value of σ_{tot}^{sp} at the southern most location in the plot.] Qualitatively, the associated rise in RCS can be understood by the sharp decrease in the cross-front divergence in a manner that is also

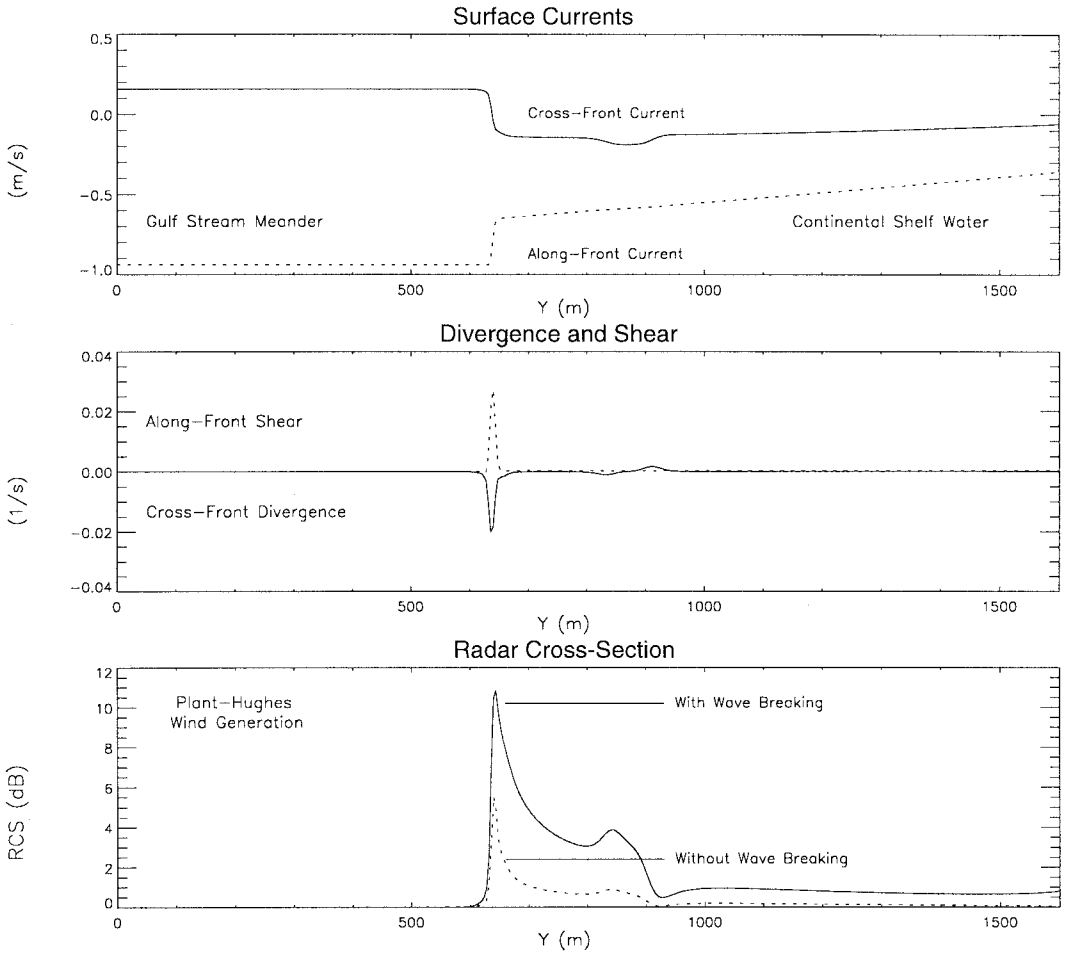

Fig. 3. Plots of surface currents (top panel), corresponding divergence and shear (middle panel), and RCS (bottom panel) with and without the WB correction, derived from the LWBC procedure, as a function of position, derived at a particular, representative time (T_2) in the evolution of the subsurface current simulation, as discussed in [7]. The cross-front (northward) current V is plotted using a solid line. The along-front (westward) current ($= -U$) is plotted with a dashed line. (The westward component $= -U$ is plotted, as opposed to the eastward component $= U$, so that the two current components can be readily displayed in a single plot.) The associated cross-front divergence ($\partial v/\partial y$), also referred to as the strain rate in the text, is plotted with a solid line. The associated along-front shear ($-\partial u/\partial y$) is plotted with a dashed line. Values of the RCS with and without the WB correction, respectively, are plotted using solid and dashed lines.

found in the alternative 1-D model [3], [4]. This enhancement (as well as some of the additional structure to the right of the enhancement [7]) also qualitatively can be understood by applying the relaxation model [26]. In [7], a discussion is provided of the relationship between the CB RCS and the underlying current structure.

As can be seen from Fig. 3, however, in the CB model, the magnitude of the signature $\sim$5.8 dB [=maximum value of $10 * \log_{10}(\sigma^{sp}_{tot}/\sigma^{sp}_{tot}(0))$] is significantly underestimated. By incorporating the LWBC correction, the variation in the cross section increases from 5.8 to 10.9 dB. The WB-induced enhancement shown in this plot corresponds to the value $\Lambda_c = 0.4$ g. This Λ_c-value results in the largest RCS signature.

In practice, as in [7] and [10], this value, as well as the remaining values associated with the 2-D HIRES-1 simulation and in the 1-D GS'90 simulation, are determined through a number of calculations involving different values of Λ_c, which were performed to find the particular value that maximizes the variation in RCS across each front. This value for $\Lambda_c = 0.4$ g as well as the other values that are obtained ($\Lambda_c = 0.42$ g for the 2-D HIRES-1 model and $\Lambda_c = 0.375$ g for the GS'90 feature 1-D model calculations) agree with independently measured values derived from wave-tank and field measurements. Fig. 4 shows a plot of RCS for three different values (0.3, 0.4, and 0.5 g) of Λ_c for the HIRES-1 feature that illustrates the behavior of the signature as Λ_c is varied. As discussed in [7], the behavior of the RCS as a function of Λ_c is governed by a delicate balance between 1) enhanced WB from increases in $P(x, y)$ in regions away from the convergence when Λ_c is small and 2) reduced WB everywhere that results when $P(x, y)$ is diminished as a result of Λ_c being too large. The maximum value $\Lambda_c = 0.4$ g results from the balance between these competing effects.

Fig. 5 shows a plot of RCS from the LWBC method. Also shown is the comparable SBM result (based on the corresponding, calculated value of α^o) that results from (20). As can be seen from the plot, the agreement between the shapes, locations of maxima and minima, and widths of the RCS's as functions of position of the two models is good. Although immediately in the vicinity of the rip, there is a significant ($\sim$2.5 dB) enhancement, locally, of the LWBC cross-section σ_{LWBC} (in agreement with experiment) relative

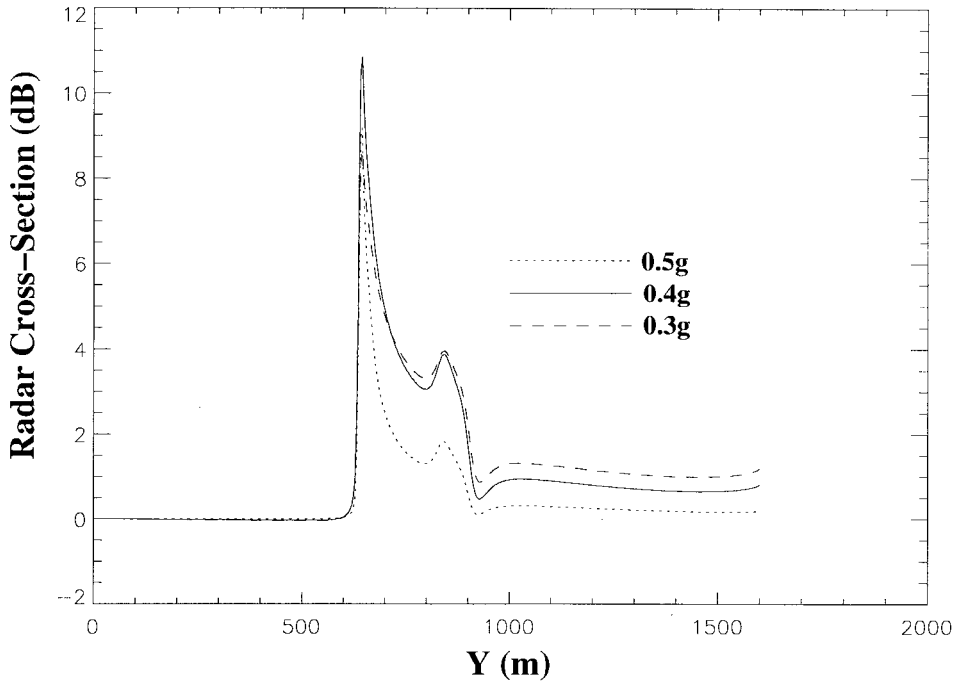

First High Resolution Remote Sensing Experiment

(HIRES–1)

Fig. 4. Plots at the same time (T_2) of the current simulation [7] of the RCS with the LWBC correction included for three different values, 0.5, 0.4, and 0.3 g, of the critical crest acceleration Λ_c. Different line styles (dashed, solid, or dotted), as labeled in the legend within the figure, are used in each RCS plot to distinguish the different values of Λ_c that are used.

to the comparable SBM cross-section σ_{SBM}; this enhancement is accompanied by a reduction (by ∼0.5–1 dB), beginning ∼100 m to the north of the rip. As a consequence, averaged spatially over the region where both models predict appreciable ($\gtrsim$0.5 dB) RCS, good agreement between the resulting mean values of the RCS is found. (Respectively, the mean RCS values are 3.94 and 4.09 dB for the LWBC and SBM methods.) Also, the calculated value, 1.03 dB, for the rms deviation associated with the comparably averaged difference between the computed LWBC and SBM cross sections is relatively small. Additional similarities and differences between the SBM and LWBC model results are discussed in [7].

Fig. 6 shows polarimetrically resolved, H-V (H-transmit and V-receive) and V-V images taken by the Jet Propulsion Laboratory AIRSAR during GS'90, for C-, L-, and P-band (5.2, 1.25, and 0.44 GHz) frequencies. This figure illustrates the frequency and polarimetric dependencies of both the "velocity" and "temperature" front signatures, which, respectively, appear as vertical lines toward the northern and southern portions of the figure. Of interest to us in this paper is the brighter and narrower signature that occurs on the southern side (to the right) in each image. It is quite clear from the figure that the signature exhibits important sensitivities with respect to frequency and polarization. In a separate study [27], these dependencies have been investigated using a polarimetric analysis procedure for extracting surface slope asymmetries and a similar theoretical model to the one presented here, based on the SBM. This other study is primarily concerned with V-V- and H-V-polarizations at L- and P-band. Because the physical optics approximation is assumed in the version of the LWBC model that has been developed in the present paper, this model can only be applied when $2\pi H(\boldsymbol{r})/\lambda \gg 1$ ($\lambda \equiv$ radar wavelength). For the values of $H(\boldsymbol{r})$ that are relevant in the present study, this inequality breaks down in the vicinity of the feature for these frequencies. For this reason, the model cannot be applied to these cases. The model does apply, however, for C-band.

Fig. 7 shows the RCS along a 1-D cut across the front, averaged in the vertical direction over 50 adjacent lines to reduce speckle. The location of largest variation (∼2.2 dB) occurs with H-V-polarization. Because (6) and (7) have not been derived for H-V polarization, it is not clear if (8) holds for this case. For this reason, the result of applying (11) to this polarization may require refinement. Also, (6)–(8) are not valid for P- and L-Band.

Fig. 8 shows a plot of the currents [based on (1) and (2)] that are used to model the GS'90 feature (top panel), the resulting shear and divergence, and simulated height $H(\boldsymbol{r})$ that results when the resulting solution for F is substituted into (18). As in the HIRES-1 case, by construction, it is to be expected that the largest return occurs at the location where the

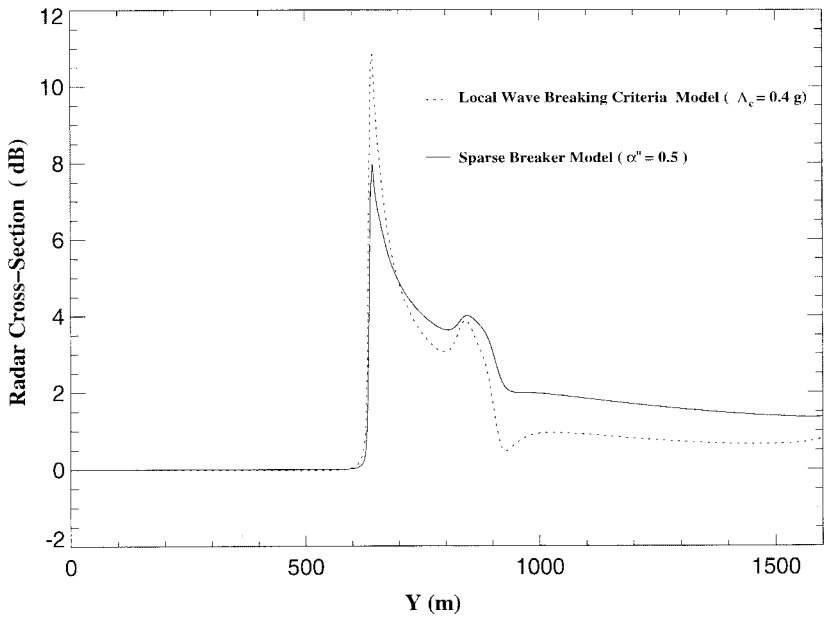

Fig. 5. Plots of the RCS based on the LWBC method (dotted line) and SBM (solid line), as a function of position, for the particular values of Λ_c (=0.4 g) and α^o (=0.5) that maximize the WB-induced enhancement. This value of Λ_c, for the model that is considered, also provides the optimal agreement between simulation and experiment for the maximal variation in RCS.

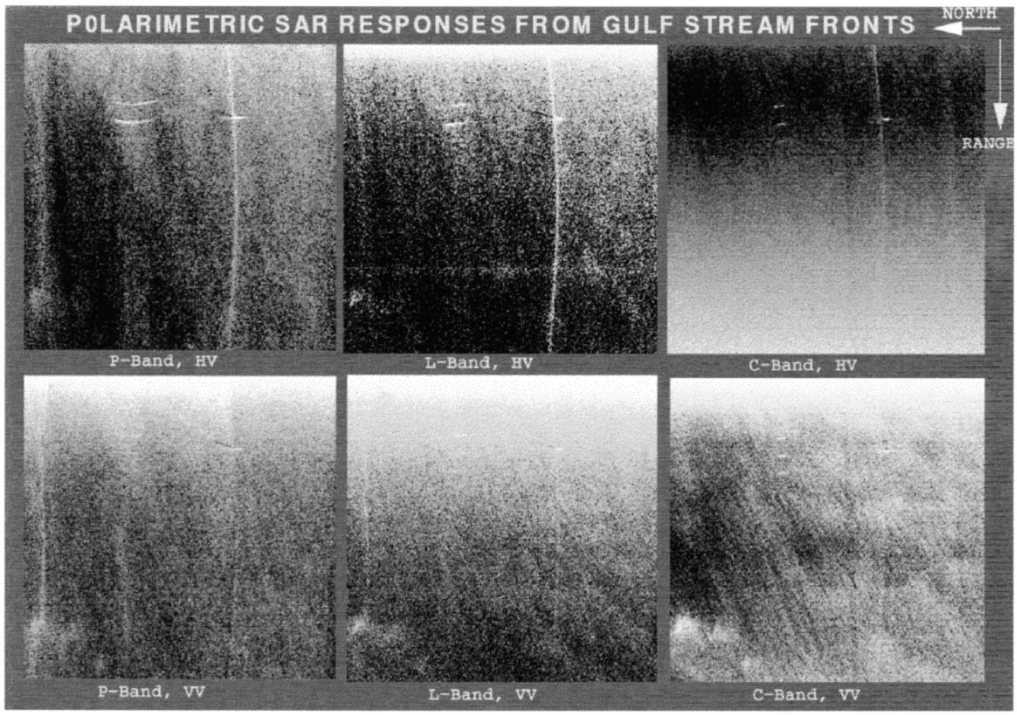

Fig. 6. Synthetic aperture radar (SAR) images with H-V- (H-transmit and V-receive) and V-V-polarization, taken by the Jet Propulsion Laboratory AIRSAR during GS'90, for C-, L-, and P-band (5.2, 1.25, and 0.44 GHz) frequencies, as marked. The particular flight path is shown in [2] (Pass SS 360-1). North is toward the left. The AIRSAR was flying from south to north. The data have been averaged by a multilook factor of 16 (16-look processing). The "temperature front" as in [12] is to the south (right) in each image.

divergence ($\equiv$negative convergence) achieves its minimum. This is confirmed in the top plot of Fig. 9, which shows plots of the resulting simulated H-H polarization RCS (for C-band with 45° angle of incidence) with and without the WB-induced enhancement that results from applying the LWBC method. As can be seen from this plot, the CB model prediction for the RCS signature is only $\sim$0.15 dB; while in the presence of WB, the simulated signature is $\sim$2.8 dB. This last value is somewhat larger than the comparable ($\sim$1.2 dB, C-Band, H-H) signature that is apparent in the middle of the comparable plot in Fig. 7. This WB-induced enhancement corresponds to the value $\Lambda_c = 0.375$ g, which occurs at the maximum WB-induced enhancement in RCS. The bottom of Fig. 9 shows a plot of RCS for three different values (0.375, 0.45, and 0.3 g) of Λ_c that illustrates how the RCS varies as a function of Λ_c. As can be seen from the plot, the variation in RCS is not

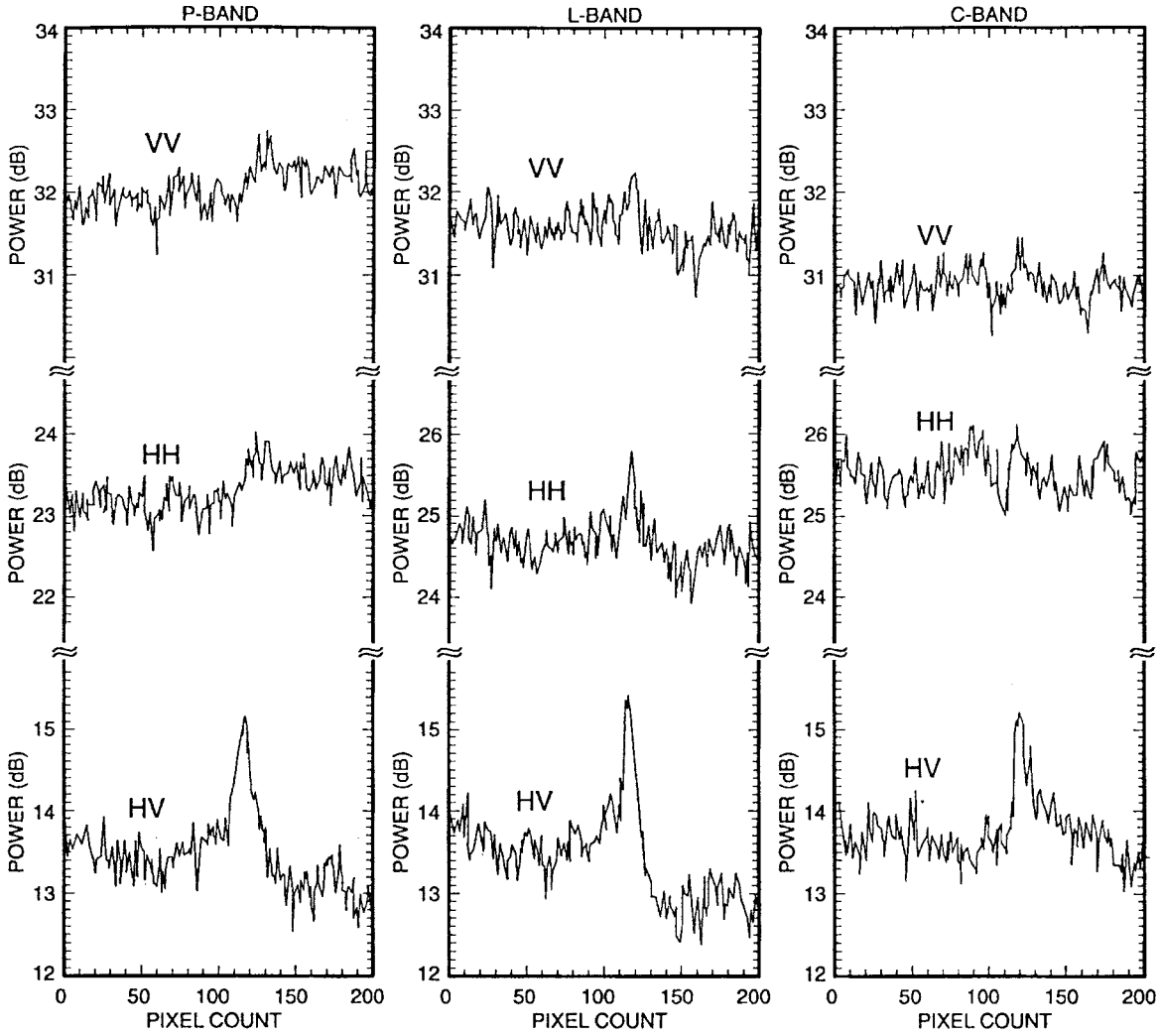

Fig. 7. Shows an average of the RCS (relative power, dB) along a representative 1-D cut across the GS'90 "temperature front," for L-, P-, and C-band frequencies and V-V-, H-V-, and H-H-polarizations. The average was taken over 50 adjacent lines parallel to the cut. The horizontal axis refers to the relative position, in which pixel count is a relative measure of north–south location: the separation between pixels is 12 m. The "temperature front" occurs at pixel count 100. The location of largest variation (∼2.5 dB) occurs with H-V-polarization.

as nearly pronounced in this plot as Λ_c is varied, as it is in Fig. 4. The reason for this is that the wind speed (∼8 m/s) in the GS'90 case is considerably larger than in the HIRES-1 case. Because of this difference in wind speed, the ambient WB-induced enhancement in RCS is considerably larger in the GS'90 case than in the HIRES-1 case. This is the reason the GS'90 signature is less sensitive to variations in Λ_c. The simulated value for the CB model H-V polarization, C-Band RCS signature is 1.2 dB. When the value $\Lambda_c = 0.375$ is used in (11), this variation increases to ∼2.2 dB.

C. 2-Dimensional Model Results

Using the sinusoidally varying, 2-D model (5) for the northward current component V, we have used the procedure outlined in Section II to derive the associated wave spectrum and RCS, with and without WB. To obtain the WB enhancement, we fixed Λ_c by determining the maximum value of the enhancement. [For this case, the ambient value of the RCS is assumed to be the minimum value $\sigma_{tot}^{sp}(\min)$ of the RCS that results from the simulation, and the enhancement is expressed in decibels.] As noted above, using this procedure, we have obtained the estimate $\Lambda_c = 0.42$ g, which agrees well with the other two critical crest acceleration estimates.

Fig. 10 shows plots of the RCS with [Fig. 10(b)] and without [Fig. 10(a)] WB when the radar is pointed across the rip. The signature of the rip appears as the meandering sinusoidally varying region of large RCS variation found in the center of each plot. The largest RCS variations (∼15–18 dB) are found in the regions of large variation located in the "cusp-like" positions (marked by arrows) within the signature in both plots. The smallest variations in RCS within the signature in each case are found in the "noncusp-like" regions (also marked by arrows). In the non-WB case [Fig. 10(a)], this minimal RCS variation (within the noncusp-like portion of the signature), relative to the minimal RCS value (found far from the signature) is ∼6 dB; while in the cusp-like region, the comparable RCS-variation is 16 dB. Although experimentally [5], [6] in comparable "cusp-like" regions, large ∼15 dB variations in RCS were observed, variations in RCS of ∼10 dB were observed in the noncusp-like regions. As a result, when the CB

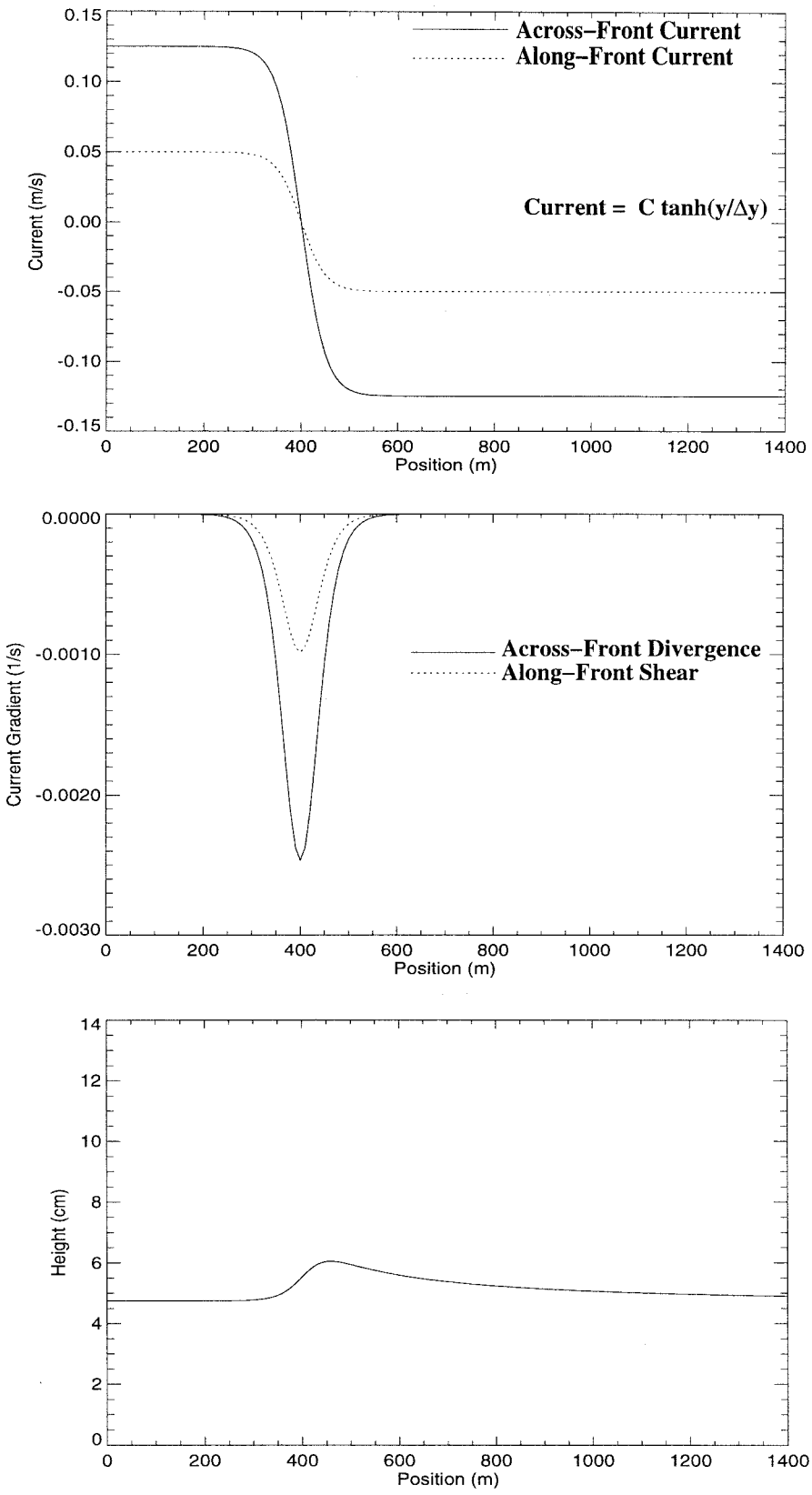

Fig. 8. Shows a plot of the currents [based on (1) and (2)] that is used to model the GS'90 feature (top panel), the resulting shear and divergence, and simulated height $H(\boldsymbol{r})$ that results when the resulting solution for F is substituted into (18). Currents, shear, and divergence ($\equiv -(\partial V/\partial y)$ are defined as in Fig. 4.

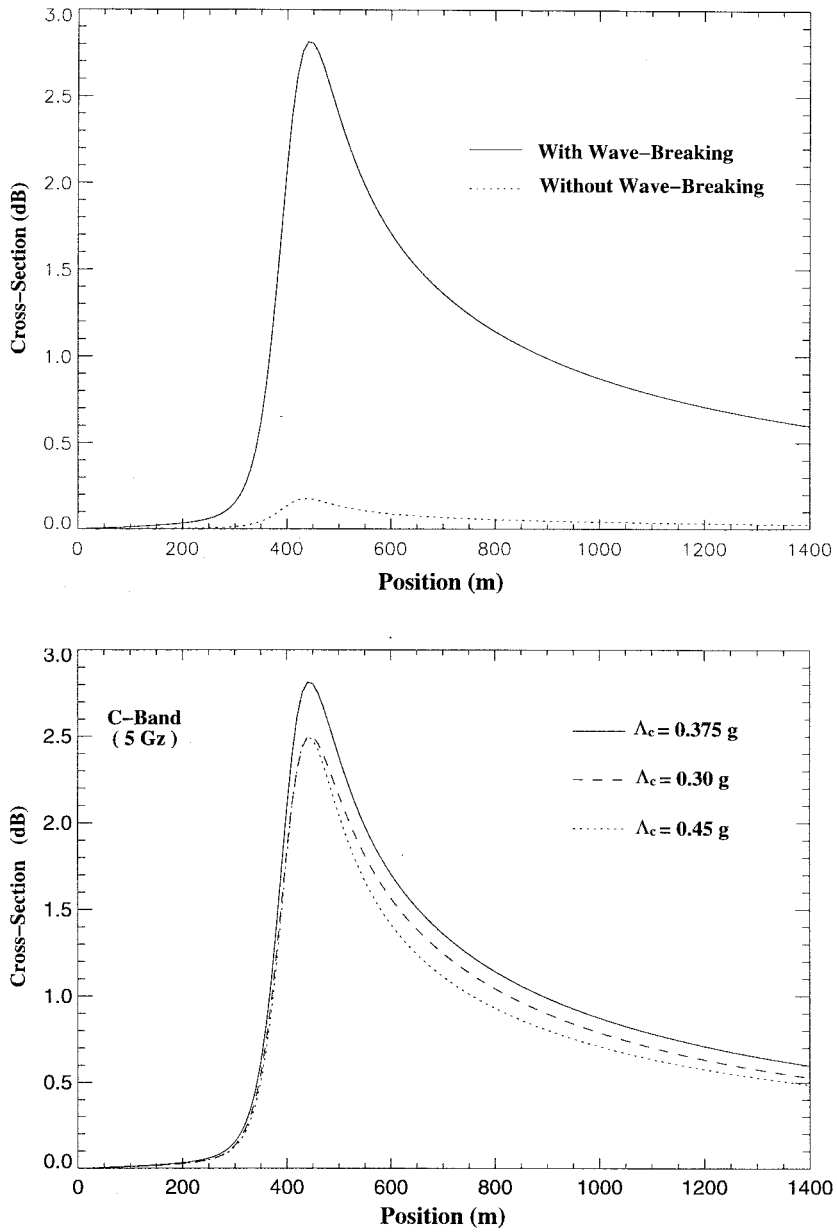

Fig. 9. Shows plots, as a function of position, of simulated GS'90 RCS (for C-band and H-H polarization, with 45° angle of incidence) with and without the WB-induced enhancement that results from applying the LWBC method (top plot) and dependence of GS'90 RCS on critical crest acceleration Λ_c (bottom plot), for three values of $\Lambda_c = 0.3$, 0.375, and 0.45 g. In each plot, RCS is measured in decibels, relative to the minimal RCS value, which occurs at the extreme left (southern) boundary of the plot. As can be seen from this plot, the CB model prediction for the RCS signature is only ∼0.15 dB; while in the presence of WB, the simulated signature is ∼2.8 dB. In each case, north is directed toward the right along the x-axis.

model is used alone, a considerably larger range of variation (∼6–16 dB) in RCS is obtained from modeling within the rip than was observed. Considerable improvement [as can be seen in Fig. 10(b)] is obtained when the WB effect is included. For this case, we find that in the cusp-like and noncusp-like regions, respectively, the RCS varies by ∼17 and ∼12 dB. Thus, by including two-dimensionally varying currents, it is found that, when the radar is pointed across the rip, significant (∼15–18 dB) variations in RCS are obtained in the cusp-like regions of the rip, regardless of whether WB effects are included. This variation in RCS is significantly larger than the comparable variation that is obtained in noncusp-like regions. Both of these trends agree with experimental observation. However, without WB, the range (∼6–16 dB) of variation in RCS-values within the signature is considerably larger than is observed experimentally. By incorporating WB, it is found that this deficiency is eliminated and quantitative agreement is obtained.

WB effects are also found to be important in our ability to simulate the look angle dependence. Without WB effects, the RCS exhibits a sensitivity with respect to changes in look-angle that was not found experimentally; when WB effects are included, this deficiency is eliminated. This effect is illustrated in Fig. 11(a) and (b), where simulated plots of RCS are shown when the radar is pointed along the rip (i.e., perpendicularly to the dominant current convergence). By comparing this plot with Fig. 10(a) and (b), we find that the signature effectively disappears in simulations that do not incorporate the WB

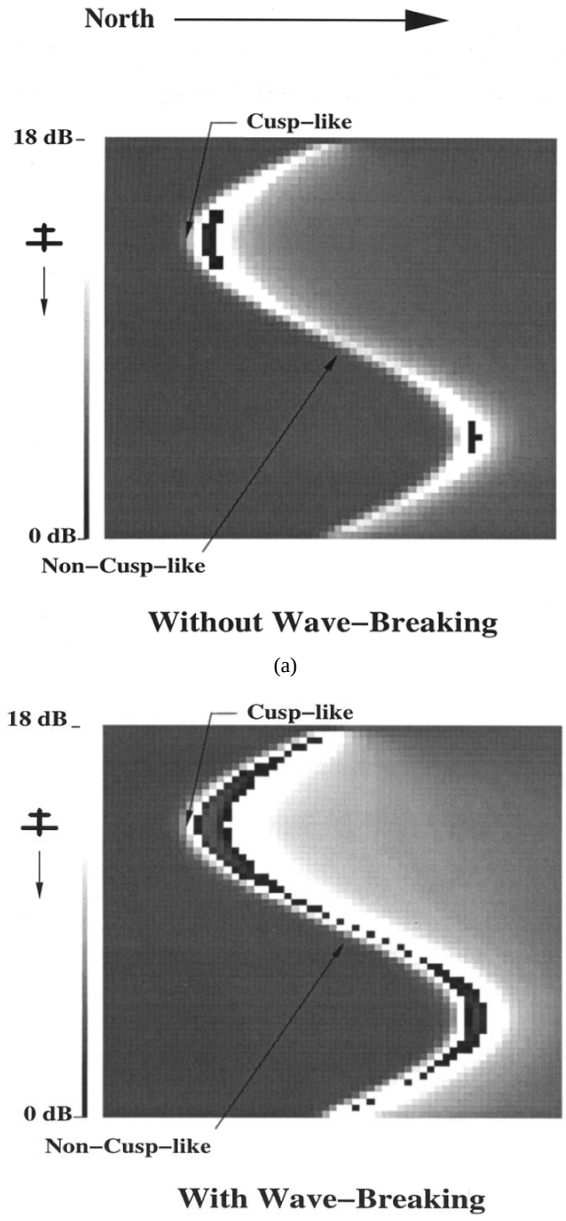

Fig. 10. Simulated RCS values, looking across HIRES-1 rip feature, (a) without and (b) with WB enhancement (computed from the LWBC procedure with the value $\Lambda_c = 0.42$ g that maximizes the WB enhancement), in decibels (as marked), relative to the minimum value associated with each plot. The schematic of the airplane is used to indicate the flight path in each plot. "Cusp-like" ("noncusp-like") regions (marked by arrows) refer to regions where the signature is strongly (weakly) dependent on 2-D variations in position within the rip. "Cusp-like" ("noncusp-like") regions, here and (qualitatively) in Fig. 1, show the greatest (least) variation in enhancement in RCS within the rip.

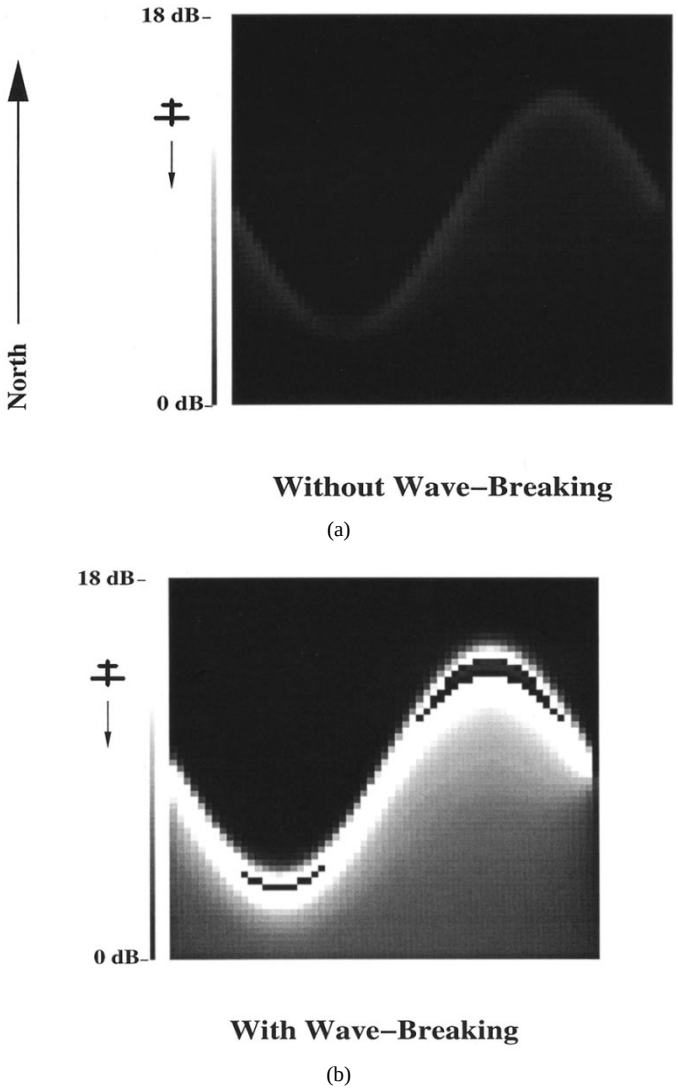

Fig. 11. Simulated RCS values, looking along rip, (a) without and (b) with WB (again based on the LWBC procedure with the value $\Lambda_c = 0.42$ g), in decibels (as marked), relative to the minimum value of the RCS obtained in each plot. The schematic of the airplane is used to indicate the flight path in each plot.

effect, while for cases in which WB is included, the signature closely resembles the comparable signature that is obtained when the radar is pointed across the rip.

IV. Summary

In this paper, we have documented the full spectrum procedure that has been used to simulate radar signatures that were observed during HIRES-1 and GS'90. Because, as in earlier calculations, in the absence of WB, we have found that the simulations significantly underpredict the magnitude of both signatures, we have introduced an approximate model for simulating the effects of WB on radar backscatter. Our motivation for doing this was two-fold: 1) the initial model does not include these effects and 2) WB was observed in the vicinity of each feature. The new approach, which we have named the LWBC method, effectively marries a more restrictive, deterministic method for modeling WB effects by Wetzel with a statistical scheme. We have also illustrated how this LWBC procedure can be related to an earlier (less quantitative) procedure, called the SBM [3], [4], [7], for including WB effects. Three key results of the analysis include the following:

1) LWBC procedure has a single adjustable parameter, critical crest acceleration Λ_c, which can be adjusted to provide the desired signature;
2) resulting estimates of Λ_c seem to be applicable in very different situations, involving very different environmental forcing from the currents and winds;

3) using the LWBC procedure, quantitative agreement for the magnitude of both signatures can be obtained.

The value of Λ_c that results $\sim$0.4 g agrees well with independent measurements and is within the theoretically possible range that is bounded by the Stokes wave value $\Lambda_c = 0.5$ g. The fact that the value $\Lambda_c \sim 0.4$ g obtained in the present study agrees with independent measurements of this quantity and does not seem to be affected by the changes in environmental forcing used in the modeling suggests that our procedure for inferring this parameter provides independent evidence that the probability for WB can be related to Λ_c. This result also suggests that our procedure provides a useful method for inferring critical crest acceleration.

We have found that incorporation of WB not only improves the quantitative agreement between simulated and measured values of the signatures, it also eliminates additional deficiencies in the modeling. In particular, by including WB in a 2-D model of the HIRES-1 rip, very good agreement with experiment is obtained for the magnitude of the signature across and within the rip. Thus, within the rip, when WB effects are included, the location of maximal and minimal cross section, and the manner in which RCS varies within the meander all agree well with the experiment. Also, incorporation of these effects into the RCS modeling eliminates the nonphysical dependence on look-angle that occurs when the CB model is used alone.

ACKNOWLEDGMENT

The authors acknowledge valuable discussions with T. L. Ainsworth, G. R. Valenzuela, and C. Y. Shen. This work received support through computer time allocations, provided by the DOD High Performance Computing Modernization Plan.

REFERENCES

[1] G. O. Marmorino and C. L. Trump, "A salinity front and current rip near Cape Hatteras, North Carolina," *J. Geophys. Res.*, vol. 99, pp. 7627–7638, 1994.
[2] G. R. Valenzuela, R. P. Mied, A. R. Ochadlick, M. Kobrick, P. M. Smith, F. Askari, R. J. Lai, D. Sheres, J. M. Morrision, and R. C. Beal, "The July 1990 Gulf Stream experiment," in *Int. Geosci. Remote Sensing Symp. Digest*, 1991, vol. 1, pp. 119–122.
[3] R. W. Jansen, T. L. Ainsworth, R. A. Fusina, S. R. Chubb, and G. R. Valenzuela, in *Proc. 1994 Int. Geosci. Remote Sensing Symp.*, 1994, vol. 1, pp. 460–463.
[4] R. W. Jansen, S. R. Chubb, R. A. Fusina, J. S. Lee, G. O. Marmorino, and G. R. Valenzuela, in *Proc. 1994 Int. Geosci. Remote Sensing Symp.*, 1993, vol. 2, pp. 550–552.
[5] F. Askari, *EOS*, vol. 73, no. A3/suppl., p. 247, 1992.
[6] ——, unpublished.
[7] R. W. Jansen, C. Y. Shen, S. R. Chubb, A. L. Cooper, and T. E. Evans, "Subsurface, surface, and radar modeling of a gulf-stream current convergence," *J. Geophys. Res.*, vol. 103, pp. 18 723–18 743, 1998.
[8] R. L. Snyder and R. M. Kennedy, "On the formation of whitecaps by a threshold mechanism—Part I: Basic formalism," *J. Phys. Ocean.*, vol. 13, pp. 1482–1492, 1983.
[9] ——, "On the formation of whitecaps by a threshold mechanism—Part II: Monte Carlo experiments, *J. Phys. Ocean.*, vol. 13, pp. 1493–1504, 1983.
[10] S. R. Chubb, A. L. Cooper, R. W. Jansen, and C. Y. Shen, "An end-to-end simulation of radar signatures from the HI-RES 1 Rip Feature," *IGARSS'96 Dig.*, vol. 2, pp. 902–904, 1996.
[11] R. A. Fusina, A. L. Cooper, and S. R. Chubb, "High resolution computations of ocean wave spectral modulations due to two-dimensional wave-current interactions," *J. Comp. Phys.*, vol. 132, p. 215, 1997.
[12] G. O. Marmorino, R. W. Jansen, G. R. Valenzuela, C. L. Trump, J. S. Lee, and J. A. C. Kaiser, "Gulf stream surface convergence imaged by synthetic aperture radar," *J. Geophys. Res.*, vol. 99, p. 18 315, 1994.
[13] G. S. Brown, "Backscattering from a Gaussian-distributed perfectly conducting rough surface," *IEEE Trans. Antennas Propagat.*, vol. AP-26, p. 472, 1978.
[14] D. R. Lyzenga and J. R. Bennett, "Full-spectrum modeling of synthetic aperture radar internal wave signatures," *J. Geophys. Res.*, vol. 93, pp. 12 345–12 354, 1988.
[15] L. B. Wetzel, "Electromagnetic scattering from the sea at low grazing angles," in *Surface Waves and Fluxes Volume II—Remote Sensing*, G. L. Geernaert and W. J. Plant, Eds. Dordrecht, The Netherlands: Kluwer, 1990, pp. 146–171.
[16] ——, "On microwave scattering by breaking waves," in *Wave Dynamics and Radio Probing of the Ocean Surface*, O. M. Phillips and K. Hasselmann, Eds. New York: Plenum, 1986, pp. 273–284.
[17] M. S. Longuet-Higgins and J. S. Turner, "An entraining plume model of a spilling breaker," *J. Fluid Mech.*, vol. 63, pp. 1–20, 1974.
[18] J. A. Saxton and J. A. Lane, "Electrical properties of sea water," *Wireless Eng.*, vol. 29, pp. 269–275, 1952.
[19] A. W. Bjerkaas and F. W. Riedel, "Proposed model for the elevation spectrum of a wind-roughened surface," Rep. TG-1328, Appl. Phys. Lab., Johns Hopkins Univ., Laurel, MD, 1979.
[20] D. R. Thompson, "Calculation of radar backscatter modulations from internal waves," *J. Geophys. Res.*, vol. 93, pp. 12 371–12 380, 1988.
[21] D. R. Thompson, B. L. Gotwols, and W. C. Keller, "A comparison of K_u Band Doppler measurements at 20° incidence with predictions from a time-dependent scattering model," *J. Geophys. Res.*, vol. 96, pp. 4947–4955, 1991.
[22] D. R. Thompson and B. L. Gotwols, "Radar backscatter probability density functions," *J. Geophys. Res.*, vol. 99, pp. 9725–9739, 1994.
[23] D. R. Lyzenga, private communication, 1995.
[24] M. S. Longuet-Higgins, "The generation of capillary waves by steep gravity waves," *J. Fluid Mech.*, vol. 16, pp. 138–159, 1963.
[25] B. Kinsman, *Wind Waves*. Englewood Cliffs, NJ: Prentice-Hall, 1965, pp. 336–341.
[26] W. Alpers and I. Hennings, "A theory of the imaging mechanism of underwater bottom topography by real and synthetic aperture radar," *J. Geophys. Res.*, vol. 89, pp. 10 529–10 546, 1984.
[27] J. S. Lee, R. W. Jansen, D. L. Schuler, T. L. Ainsworth, G. O. Marmorino, and S. R. Chubb, "Polarimetric analysis and modeling of multi-frequency SAR signatures from Gulf Stream fronts," *IEEE Ocean Sci. Eng.*, vol. 23, p. 322, 1997.

Scott R. Chubb was born on January 30, 1953, in Manhattan, NY. He received the B.A. degree in physics from Princeton University, Princeton, NJ, in 1975 and the M.A. and Ph.D. degrees, also in physics, from the State University of New York (SUNY) at Stony Brook, in 1978 and 1982, respectively. His dissertation in the area of theroetical solid state physics and surface science was carried out primarily at Brookhaven National Laboratory, Upton, NY.

From 1982 to 1989, he primarily worked on problems associated with the electronic structure and magnetic properties of surfaces, interfaces, and alloys, first, as a Research Associate (from 1982 to 1985) at Northwestern Univeristy, Evanston, IL, and then, while in residence at the Naval Research Laboratory (NRL), Washington, DC, as a National Research Council Fellow (1985 to 1988), and as an employee of Sachs/Freeman Associates, Inc., Landover, MD (between 1988 and 1989). Beginning in 1988, he also began work in areas related to applications of microwaves in space technology at NRL. He became an employee of NRL in 1989. Besides being a permanent NRL employee, concurrently he has held consultant positions with Research Systems, Inc., Arlington, VA, since 1990, and Oakton International Corporation, Oakton, VA, since 1995, in areas related to cold nuclear fusion. His research interests include microwave sensing of the ocean, applications of relativity in the maintenance of precision time in space, and the study of hydrogen in metals and its implications in cold nuclear fusion. He has been an author of more than 50 refereed publications in scientific journals, in areas related to solid state physics, general and special relativity, electromagnetic scattering, nonlinear wave dynamics, statistical physics, and nuclear physics. He is an author of one patent (awarded in 1996) for a device that eliminates navigational errors in the global positioning system (GPS) from the effects of the sun on GPS microwave transmissions, and of two pending, process patents associated with cold nuclear fusion.

Arnold L. Cooper received the B.M.E. degree in mechanical engineering from the City College of New York in 1958, the M.S. degree in mechanical engineering from The Ohio State University, Columbus, in 1961, and the M.A. and Ph.D. degrees in aerospace and mechanical sciences from Princeton University, Princeton, NJ, in 1971.

He is a Research Physicist in the Remote Sensing Division of the Naval Research Laboratory, Washington, DC, where he has been since 1971. His current research interests have been concerned with the study of oceanographic features and their remote sensing. From 1966 to 1969, he was employed as a theoretical aerodynamicist at the General Electric Space Sciences Laboratory where he performed theoretical studies in rarefied gas dynamics related to the atmospheric reentry problem. From 1969 to 1971, he was involved in studies of boundary layer separation on wings at the Grumman Aerospace Corporation. Prior to his current work in the Remote Sensing Division, he began his tenure at the Naval Research Laboratory in the Plasma Physics Division, where he was involved in studies of the stability of high energy density implosions associated with plasma and magnetic flux compression. He spent two years (1987–1988) at the Office of Naval Research as Director of Laboratory Liaison, where he managed the Navy Laboratory Independent Research Program.

Robert W. Jansen was born in Mankato, MN, on October 4, 1959. He received the B.S. degree in mathematics and physics from Mankato State University in 1981. In 1987, he received the Ph.D. degree in theoretical solid state physics from Arizona State University, Tempe.

From 1987 to 1989, he was a Postdoctoral Associate in the Condensed Matter and Radiation Science Division, Naval Reseach Labhoratory (NRL), Washington, DC. He worked at Dynamics Technology from 1989 to 1991, where he became interested in remote sensing. Since January 1991, he has been with the Remote Sensing Division of the NRL. His research efforts have encompassed a broad range of topics. In the area of solid state physics he has made numerous contributions to the understanding of the electronic structure and energetics of defects in semiconductors. Since 1990, he has been primarily involved in research relating to synthetic aperture radar (SAR) remote sensing. He has made contributions to wave-current interaction on surrface wind waves, bathymetry prediction from radar, target classification both on land and open ocean SAR imagery, and other aspects related to SAR imaging.

Robert A. Fusina received the B.S. degree in physics from Manhattan College, Bronx, NY, in 1983, and the M.S. and Ph.D. degrees in physics from the State University of New York, Albany, in 1986 and 1988, respectively.

He was an Office of Naval Technology Postdoctoral Fellow at the US Naval Research Laboratory (NRL), Washington, DC, from 1989 to 1992 in the Condensed Matter and Radiation Sciences Division. Since 1992, he has worked in the Remote Sensing Division of NRL, first as an Allied Signal Technical Services contract employee (1992–1993) and then as a government employee since 1993. His interests include electromagnetic scattering from the ocean surface, fluid dynamics, image processing, and remote sensing.

Jong-Sen Lee (S'66–M'69–SM'91–F'97) received the M.A. and Ph.D. degrees from Harvard University, Cambridge, MA, in 1965 and 1969, respectively.

Since then, he has been with the US Naval Research Laboratory (NRL), Washington, DC, where he is presently the Head of the Image Science Section, Remote Sensing Division. He is also the principal investigator for several remote sensing programs on polarimetric SAR and interferometric SAR. He developed several speckle filtering algorithms, that have been implemented in many Gi, such as ERDAS, PCI, ENVI, etc. His research covers a wide spectrum of areas from control theory, operation research, and radiative transfer, to SAR and polarimetric SAR image processing. He has investigated SAR image segmentation, inverse SAR, polarimetric SAR imagery statistics and speckle filtering, and terrain/target classification and applications. His current research interests are in the area of multi-frequency polarimetric decomposition, terrain classification, scattering signature modeling, SAR interferometry, and SAR and HSI data fusion.

Dr. Lee is a Fellow of the IEEE for his contribution to information processing of SAR and polarimetric SAR imagery. He has chaired and organized many sessions in international conferences.

Farid Askari received the B.S. degree in engineering from Purdue University, West Lafayette, IN, in 1977, and the M.S. and Ph.D. degrees in 1979 and 1985, respectively, in remote sensing and physical oceanography from the The Ohio State University, Columbus, and North Carolina State University, Raleigh.

Fron 1988 to 1997, he was with the US Naval Research Laboratory, Washington, DC, as a Research Physicist. In 1997, he joined the Saclant Undersea Research Centre, La Spezia, Italy, as a principal scientist and the remote sensing coordinator for NATO's Rapid Response exercises. Since 1980, he has been working in the area of remote sensing, image processing, and pattern recognition, and has served as principal investigator on several international projects. His current research interests include sensor fusion, and development of rapid environmental assessment tools using satellite remote sensing imagery.